Rare Metal Materials and Engineering
Volume 52, Issue 3, March 2023
Available online at www.rmme.ac.cn

Science Press

Cite this article as: Teng Haihao, Xia Yufeng, Sun Tao, et al. Flow Stress Prediction of Near-β Ti-55511 Alloy During Isothermal Compression Based on Corrected Arrhenius Model with Material Parameter Evolution and BP-ANN Model[J]. Rare Metal Materials and Engineering, 2023, 52(03): 823-833.

ARTICLE

Flow Stress Prediction of Near-β Ti-55511 Alloy During Isothermal Compression Based on Corrected Arrhenius Model with Material Parameter Evolution and BP-ANN Model

Teng Haihao, Xia Yufeng, Sun Tao, Zheng Deyu, Chen Lei

College of Materials Science and Engineering, Chongqing University, Chongqing 400044, China

Abstract: To investigate the hot flow behavior of Ti-55511 alloy in near-β region, isothermal compression tests were conducted at the temperature of 973−1223 K and the strain rate of 0.001−1 s^{-1} by Gleeble-3500 thermomechanical simulation equipment. The flow stress curves obtained from experiments were corrected, and the influence of friction and adiabatic temperature rise on flow stress was reduced. The corrected Arrhenius model with consideration of material parameter evolution and the back-propagation artificial neural network (BP-ANN) model were used for flow stress prediction of Ti alloys during hot deformation process, and the precision of these prediction models were evaluated by statistical analysis. The stress and strain data extended by the two prediction models were implanted into finite element to simulate the hot compression process. Results show that the flow stress of Ti-55511 alloy has a positive correlation with strain rate and a negative correlation with temperature. The alloy softening mechanism is primarily the recrystallization. Both the corrected Arrhenius model and BP-ANN model can describe the flow behavior of fluid, and the fitting accuracy of BP-ANN model is higher than that of corrected Arrhenius model in α+β region but lower than that of corrected Arrhenius model in β region.

Key words: constitutive model; Ti-55511 alloy; flow stress; corrected Arrhenius model; BP-ANN model

Due to their excellent corrosion resistance, fracture toughness, and high-temperature mechanical properties, titanium alloys are widely used in aerospace, biomedical, and chemical industries[1–4]. Because of the high yield strength and large springback, titanium alloys can hardly be processed at room temperature[5–7]. Usually, they are heated to high temperature before plastic deformation[8–10].

Near-β titanium alloys (Ti-10V-2Fe-3Al and Ti-5Al-5Mo-5V-3Cr) have high specific strength ratio and good oxidation resistance[11–13]. Generally, the dual-phase titanium alloys are produced through hot working in α+β region at β-transus (β_t) temperature from −50 °C to −20 °C and above β_t temperature from 5 °C to 30 °C[14–17]. This temperature region is called as the near-β region[18–19]. Commonly, titanium alloys undergo various interconnecting metallurgical phenomena during plastic processing at near-β region, which results in complex microstructure evolution, thereby significantly affecting the mechanical properties[20–21]. In addition to work hardening, dynamic recovery, and dynamic recrystallization, the phase transformation can also affect the properties of titanium alloys. At high temperatures, titanium alloys are mainly composed of β phase of body-centered cubic (bcc) crystal structure. With the deformation proceeding, the temperature reduction of alloys causes more transformation from β phase into α phase[22] with hexagonal close-packed (hcp) crystal structure. Compared with bcc structure, hcp structure has fewer slip systems, leading to more difficulty in deformation[23–24]. Therefore, the influence of temperature, phase evolution, and alloy properties should be considered in the process design for titanium alloy production.

During the process in near-β region, the complex plastic deformation is dominant and the working parameters should be considered, including the deformation degree, strain rate, and temperature change[25–27]. Thus, constitutive modeling is of

Received date: June 07, 2022
Foundation item: National Natural Science Foundation of China (51775068)
Corresponding author: Xia Yufeng, Ph. D., Professor, College of Materials Science and Engineering, Chongqing University, Chongqing 400044, P. R. China, E-mail: yufengxia@cqu.edu.cn

Copyright © 2023, Northwest Institute for Nonferrous Metal Research. Published by Science Press. All rights reserved.

great importance to accurately describe the deformation behavior. Currently, several constitutive models are proposed. Among them, the Arrhenius model is extensively adopted[28]. In recent years, the development of back-propagation artificial neural network (BP-ANN) model provides another method to investigate the plastic behavior of alloys[29–32]. Most models consider the material parameters as constants or strain-dependent factors, whereas they can be influenced by temperature and other conditions, thereby decreasing the simulation accuracy. Therefore, establishing a constitutive model with material parameter evolution is of great significance to investigate the deformation process. In this research, an accurate and reliable model for flow stress prediction of titanium alloys in the near-β region was proposed. Ti-55511 alloy was selected for the high-temperature isothermal compression tests. Based on the experiment results, two constitutive models for the titanium alloy in near-β region were developed, and their prediction accuracy were evaluated based on error analysis.

1 Experiment

Ti-55511 alloy (Baoti Group Co., Ltd, Baoji, China) with nominal component of Ti-5Al-5Mo-5V-1Cr-1Fe was used in this research, and its chemical composition is shown in Table 1. The transition temperature of the α/β phase is 1145 K, which was obtained the metallographic observation method.

Fig. 1 shows the schematic diagram of thermal simulation process. The hot compression tests were conducted by Gleeble-3500 isothermal simulator at temperatures of 973, 1023, 1073, 1123, 1153,1173, and 1223 K under strain rates of 0.001, 0.01, 0.1, and 1 s^{-1}. The specimens with diameter of 10 mm and height of 12 mm were machined from a cast billet. Before compression, the graphite lubricant was applied on the specimen surface to minimize the friction effect. The specimens were heated to certain temperatures at 10 K/s and then held for 180 s to eliminate the temperature gradient. The total reduction was 60%, and the stress-strain data were recorded automatically during compressing process. The stress and strain data could be converted into the true stress and true strain data by Eq.(1) and Eq.(2)[33], respectively:

$$\sigma_T = \sigma_N(1 - \varepsilon_N) \quad (1)$$

$$\varepsilon_T = \ln(1 - \varepsilon_N) \quad (2)$$

where σ_N, σ_T, ε_N, and ε_T represent the nominal stress, true stress, nominal strain, and true strain, respectively.

Table 1 Chemical composition of Ti-55511 alloy (wt%)

Al	Mo	V	Cr	Fe	C	O	N	Ti
5.12	5.14	5.06	0.93	0.98	0.01	0.15	0.02	Bal.

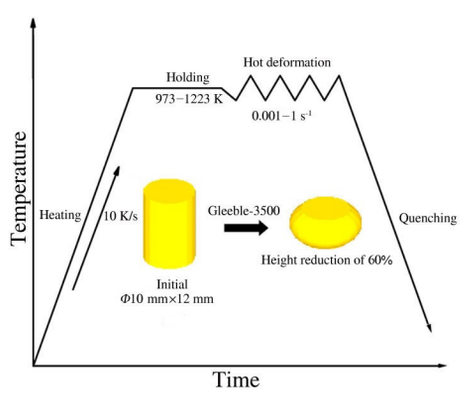

Fig.1 Schematic diagram of thermal simulation process

2 Model Establishment

2.1 Flow behavior

The true stress-true strain curves of Ti-55511 alloy under different deformation conditions are shown in Fig. 2. It can be seen that the flow stress is sensitive to the strain rate and temperature. All strain-stress curves can be divided into three stages. In the first stage, the flow stress increases dramatically, indicating the work hardening stage. In the second stage, the flow stress increases slowly to a peak value and then decreases. This is because during the early deformation, the energy stored in the grain boundaries increases. Once the energy reaches the critical value, the recrystallization nucleation occurs and causes the dynamic softening, resulting in the decreased stress. In the third stage, the flow stress has two variation trends. In $\alpha+\beta$ phase region, i.e., at 973–1123 K, the flow stress is decreased continuously with increasing the true strain. However, at 1153 – 1223 K, i. e., in the β phase region, the flow stress rapidly reaches the steady state. This is due to the α-β transformation and dynamic recrystallization. At low temperatures, a large number of α phases with a few slip systems exist in the titanium alloys. The work hardening cannot be completely offset by the dynamic recovery, so the flow stress rises. The dislocation density and the deformation distortion energy are increased with increasing the deformation. When the distortion energy reaches the critical value, the grains undergo dynamic recrystallization, leading to obvious softening phenomenon. With increasing the temperature, the nucleation of dynamical recrystallization can easily occur, and the incubation period of softening mechanism can be shortened. At high temperatures, the β phase increases, decreasing the pinning effect on dislocation. Therefore, the work hardening and softening gradually reach the dynamic equilibrium, i. e., the flow stress does not have a peak value, which is different from the phenomenon at low temperatures.

According to Fig. 2, the softening tendency of Ti-55511 alloy is more obvious at lower temperatures and larger strain rates. This is because at low temperatures, the dislocation slip and interface migration are difficult to occur. At high strain rates, the latent heat is large, which accelerates the dislocation generation rate and increases the pile-up groups. Therefore, the energy accumulation time at the grain boundary is shorter and the migration rate is slower, which finally leads to the nucleation and growth of dynamical recrystallization grains and the dislocation annihilation, significantly affecting the softening effect on titanium alloys.

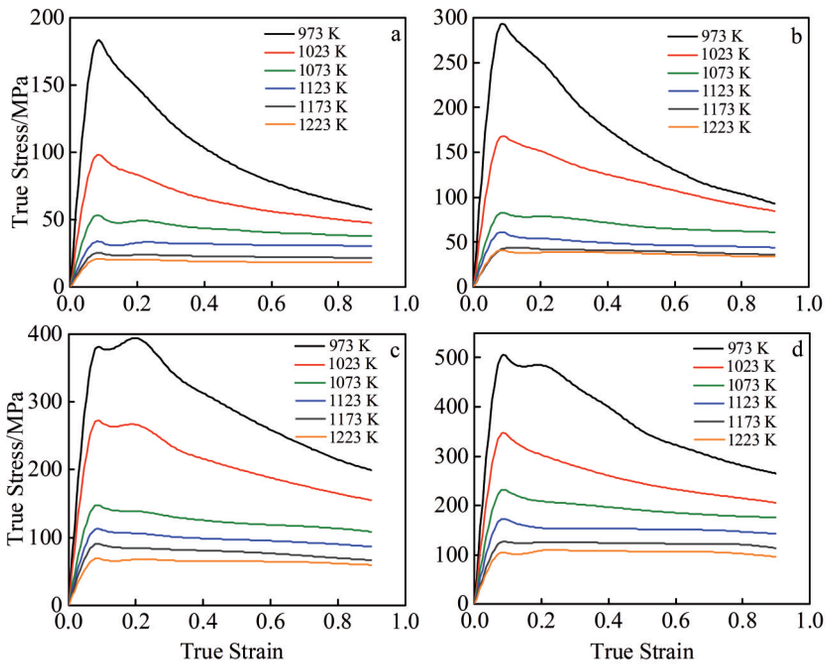

Fig.2 True stress-true strain curves of Ti-55511 alloys under different strain rates: (a) 0.001 s^{-1}, (b) 0.01 s^{-1}, (c) 0.1 s^{-1}, and (d) 1 s^{-1}

2.2 Curve correction

The establishment of constitutive model relies on the isothermal compression. In the actual compression process, the temperature changes with plastic work conversion, heat transfer, and friction, which affects the softening behavior of alloys. Therefore, it is necessary to reduce the impact of friction and temperature rise on the stress-strain curve[34]. It is found that the correction order has a slight influence on the flow stress, so it is neglected in this research.

2.2.1 Correction of deformation-induced temperature rise

The deformation-induced temperature rise ΔT is usually calculated by Eq.(3)[35–36], as follows:

$$\Delta T = \frac{0.95\eta \int \sigma \mathrm{d}\varepsilon}{\rho C_\mathrm{p}} \tag{3}$$

where 0.95 is the fraction of mechanical work conversion to heat; η is the adiabatic correction factor; ρ is the metal density ($g\cdot cm^{-3}$); C_p is the specific heat ($J\cdot g^{-1}\cdot K^{-1}$); σ is the flow stress without correction (MPa); ε is the strain. The thermodynamic simulations were calculated by JMatPro software and the results are listed in Table 2. η can be calculated by Eq.(4)[37], as follows:

$$\eta = \begin{cases} 0 & \dot{\varepsilon} \leqslant 0.001\ \mathrm{s}^{-1} \\ 0.316\lg\dot{\varepsilon} + 0.95 & 0.001\ \mathrm{s}^{-1} < \dot{\varepsilon} < 1\ \mathrm{s}^{-1} \\ 0.95 & \dot{\varepsilon} \geqslant 1\ \mathrm{s}^{-1} \end{cases} \tag{4}$$

The deformation-induced temperature rises of Ti-55511 alloys under different strain rates are shown in Fig. 3. It is found that the higher the strain rate, the larger the temperature rise. This is mainly because the low strain rate increases the deformation time, and the temperature rise caused by plastic work can disappear completely by heat exchange. On the contrary, under the high strain rate, the time for heat-exchange is less, resulting in more obvious temperature rise.

The difference between the designated and measured flow stress $\Delta\sigma$ under different conditions can be calculated by Eq.(5), as follows:

$$\Delta\sigma = \left(\frac{\partial\sigma}{\partial T_\mathrm{n}}\right)_{\varepsilon,\dot{\varepsilon}} \left(\frac{1}{\Delta T + T_\mathrm{n}} - \frac{1}{T_\mathrm{n}}\right) \tag{5}$$

where T_n is the designated forming temperature; $\dot{\varepsilon}$ is the strain rate.

2.2.2 Friction correction

Although the necessary lubrication is adopted, the friction still exists in compression tests, which changes the uniaxial deformation to the three-dimensional one, leading to the inhomogeneous deformation and a remarkable increase in flow stress. Thus, the friction correction is very important. The relationship between corrected and measured stress can be calculated by Eq.(6), as follows:

$$\sigma = \frac{\bar{\sigma}}{1 + \frac{2}{3\sqrt{3}} m \frac{r_0}{h_0} \exp\left(\frac{3\bar{\varepsilon}}{2}\right)} \tag{6}$$

where σ is the corrected stress; $\bar{\sigma}$ is the measured stress; $\bar{\varepsilon}$ is the measured strain; r_0 and h_0 are the initial radius and height

Table 2 Calculated densities and specific heats of Ti-55511 alloy by thermodynamic simulation

Temperature/K	973	1023	1073	1123	1153	1173	1223
Density, ρ/g·cm^{-3}	0.862	4.565	4.557	4.550	4.547	4.545	4.537
Specific heat, C_p/J·g^{-1}·K^{-1}	0.862	0.909	0.926	0.832	0.741	0.715	0.654

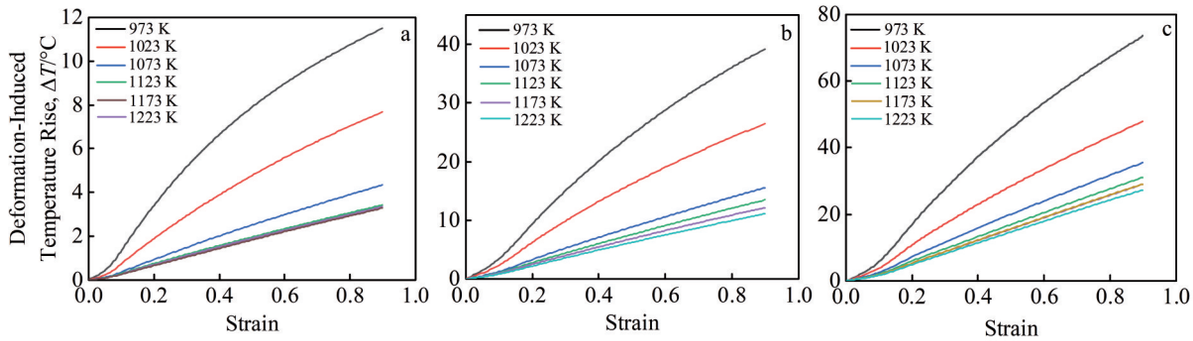

Fig.3 Deformation-induced temperature rises of Ti-55511 alloys during hot compression at different strain rates: (a) 0.01 s^{-1}, (b) 0.1 s^{-1}, and (c) 1 s^{-1}

of specimen, respectively; m is the friction factor of 0.3.

Fig. 4 shows the measured and corrected simulation true stress-true strain curves of Ti-55511 alloy under different strain rates. It can be seen that the corrected curves greatly coincide with the measured ones, and the deviation is within 16%. The biggest difference can be observed under the conditions of low temperature and high strain rate. It may be mainly attributed to strain rates. On the one hand, at higher strain rates, the adiabatic heat caused by the disappearance of plastic work leads to the large temperature rise and results in a more significant softening phenomenon. On the other hand, the high strain rate enhances the deformation inhomogeneity and reduces the force along compression direction, thereby increasing the measured stress. These two factors jointly cause errors.

2.3 Improved Arrhenius model with activation energy evolution

Due to the difference in tendency and softening mechanism between α+β phase and β phase, it is necessary to establish the corresponding constitutive models and material constants for different phases. At high temperatures, the constitutive equations of flow stress and deformation conditions can be described by the Arrhenius model containing Z parameter, as follows:

$$Z = \varepsilon \exp\left(\frac{Q}{RT}\right) = Af(\sigma) \tag{7}$$

$$\begin{cases} \sigma^{n_1} & \alpha\sigma < 0.8 \\ \exp(\beta\sigma) & \alpha\sigma > 0.8 \\ \sin(\alpha\sigma) & \text{All } \sigma \text{ is suitable} \end{cases} \tag{8}$$

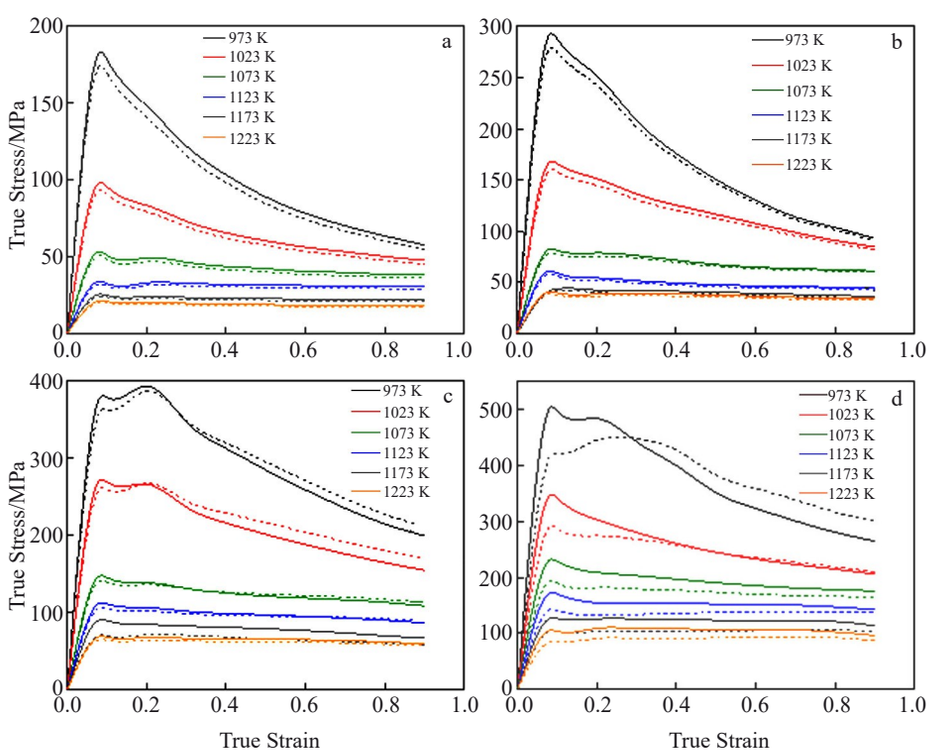

Fig.4 Initial and simulated true stress-true strain curves of Ti-55511 alloys under different strain rates: (a) 0.001 s^{-1}, (b) 0.01 s^{-1}, (c) 0.1 s^{-1}, and (d) 1 s^{-1} (solid lines indicate the initial curves; dotted lines indicate the simulated curves)

where α, β, and n_1 are alloy constants with $\alpha=\beta/n_1$; n is stress exponent (n=1/m with m as the strain rate sensitivity); Q is the activation energy of plastic deformation (J/mol); R is the gas constant; T is the temperature. The activation energy of plastic deformation Q can be obtained by Eq.(9), as follows:

$$Q = R\left\{\frac{\partial \ln \dot{\varepsilon}}{\partial \ln [\sinh(\alpha\sigma)]}\right\}_T \left\{\frac{\partial \ln [\sinh(\alpha\sigma)]}{\partial\left(\frac{1}{T}\right)}\right\}_{\dot{\varepsilon}} \tag{9}$$

In the traditional Arrhenius model, the alloy constants and activation energy are independent and non-evolutionary, or they solely evolve with strain. In this research, the constants and activation energy of Ti-55511 alloy are dependent on the compression conditions, i. e., the constants in Eq. (7) and Eq. (8) are variable and can be assumed to be functions of compression conditions ($\dot{\varepsilon}$, ε, T). Therefore, Eq. (9) can be transformed into Eq.(10), as follows:

$$\dot{\varepsilon} = A(\dot{\varepsilon}, \varepsilon, T)\sinh[\alpha(\varepsilon, T)\sigma]^{n(\varepsilon, T)} \exp\left[\frac{-Q(\dot{\varepsilon}, \varepsilon, T)}{RT}\right] \tag{10}$$

2.3.1 $\alpha(\varepsilon, T)$ function

The stress multiplier α is considered as an adjustable parameter to ensure the linear relationship of ln$\dot{\varepsilon}$-ln[sinh($\alpha\sigma$)]. Fig. 5a and 5b show the α value in $\alpha+\beta$ phase and β phase, respectively. The data are regressive-fitted to the curve surface, and the correlation coefficients R are all above 0.98. The α value curves in $\alpha+\beta$ phase and β phase can be mathematically described as Eq.(11) and Eq.(12), respectively:

$$\alpha(\varepsilon, T) = 0.156\,73 + 0.011\,15\varepsilon - 3.983\,34\times10^{-4}T - 0.008\,47\varepsilon^2 + 2.451\,9\times10^{-7}T^2 \tag{11}$$

$$\alpha(\varepsilon, T) = -0.181\,68 + 0.005\,02\varepsilon + 0.001\,97T + 0.001\,24\varepsilon^2 - 8.038\,25\times10^{-7}T^2 \tag{12}$$

2.3.2 Determination of $n(\varepsilon, T)$

Taking natural logarithm on both sides of Eq.(10), Eq.(13) can be obtained, as follows:

$$\ln\dot{\varepsilon} = \left[\frac{-Q(\dot{\varepsilon}, \varepsilon, T)}{RT} + \ln A(\dot{\varepsilon}, \varepsilon, T)\right] + n(\varepsilon, T)\ln\{\sinh[\alpha(\varepsilon, T)\sigma]\} \tag{13}$$

Then, $n(\varepsilon, T)$ can be obtained through the slope of ln$\dot{\varepsilon}$-ln{sinh[$\alpha(\varepsilon, T)\sigma$]} under different conditions. Fig.6 shows the $n(\varepsilon, T)$ value with strain and temperature. It can be seen that the $n(\varepsilon, T)$ value is decreased significantly with increasing the temperature. At a fixed temperature, $n(\varepsilon, T)$ value fluctuates with increasing the strain. Therefore, n is very sensitive to temperature and strain. The nonlinear fitting surface of $n(\varepsilon, T)$ at different temperatures and strains have the correlation coefficients of R_1=0.960 400 and R_2=0.974 651. Fig. 6 shows the n value in $\alpha+\beta$ phase and β phase. Thus, $n(\varepsilon, T)$ in $\alpha+\beta$ phase and β phase can be expressed by Eq.(14) and Eq.(15), respectively:

$$n(\varepsilon, T) = 19.916\,37 - 5.216\,84\varepsilon - 6.422\,67\varepsilon^2 - 6.656\,4\times10^{-6}T - 7.038\,25\times10^{-7}T^2 \tag{14}$$

$$n(\varepsilon, T) = 4.788\,65 - 0.206\,56\varepsilon - 0.541\,06\varepsilon^2 - 3.987\,54\times10^{-7}T - 2.026\,2\times10^{-7}T^2 \tag{15}$$

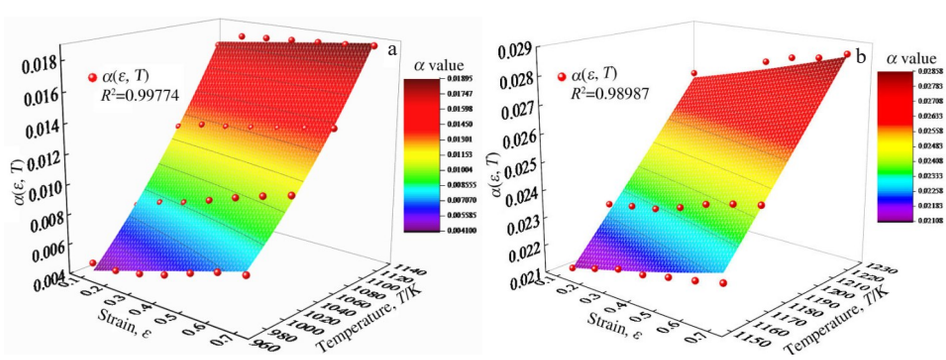

Fig.5 3D images of $\alpha(\varepsilon, T)$ values and curved surface regression fitting results in $\alpha+\beta$ phase (a) and β phase (b)

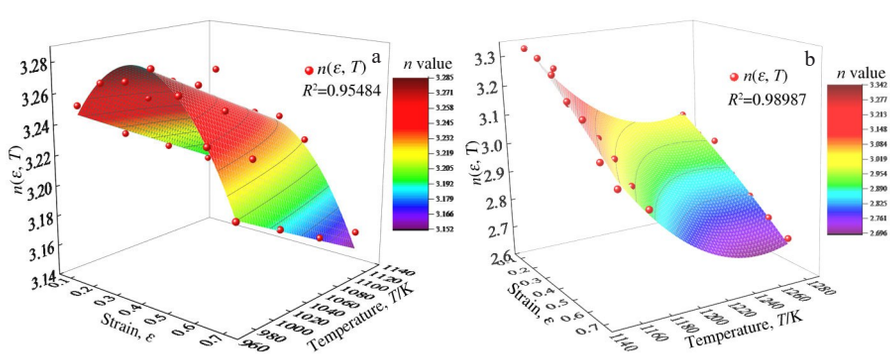

Fig.6 3D images of $n(\varepsilon, T)$ values and curved surface regression fitting results in $\alpha+\beta$ phase (a) and β phase (b)

2.3.3 Determination of $Q(\dot{\varepsilon}, \varepsilon, T)$

Under the specified strain and strain rate, Eq. (10) can be transformed into Eq.(16), as follows:

$$\frac{Q(\dot{\varepsilon},\varepsilon,T)}{Rn(\varepsilon,T)}\frac{1}{T}=\frac{\ln A(\dot{\varepsilon},\varepsilon,T)-\ln\varepsilon}{n(\varepsilon,T)}+\ln\{\sinh[\alpha(\varepsilon,T)\sigma]\} \tag{16}$$

Therefore, the activation energy Q can be obtained through the slope of $\ln\{\sinh[\alpha(\varepsilon, T)\sigma]\}$ -1/T line, as expressed by Eq.(17), as follows:

$$Q(\dot{\varepsilon},\varepsilon,T)=1000Rn(\varepsilon,T)\left\{\frac{\partial\ln\{\sinh[\alpha(\varepsilon,T)\sigma]\}}{\partial\left(\frac{1000}{T}\right)}\right\}_{\varepsilon,\dot{\varepsilon}}=1000Rn(\varepsilon,T)E(\varepsilon,\dot{\varepsilon}) \tag{17}$$

According to Eq. (17), the activation energy Q consists of two parts: $n(\varepsilon, T)$ and $E(\varepsilon, \dot{\varepsilon})$. $E(\varepsilon, \dot{\varepsilon})$ is a function of strain and strain rate, which can be obtained from the slope of $\ln\{\sinh[\alpha(\varepsilon, T)\sigma]\}$ -1000/T curve. Thus, it can be seen that $E(\varepsilon, \dot{\varepsilon})$ is increased with increasing the strain rate and fluctuates with increasing the strain, i.e., $E(\varepsilon, \dot{\varepsilon})$ is dependent on strain and strain rate. Thus, $E(\varepsilon, \dot{\varepsilon})$ is considered as a function of the strain and the strain rate in natural logarithm form in this research. Fig. 7 shows the E value in $\alpha+\beta$ phase and β phase. The correlation coefficients of E value in $\alpha+\beta$ phase and β phase are R_1=0.972 110 and R_2=0.954 753, respectively. Therefore, $E(\varepsilon, \dot{\varepsilon})$ in $\alpha+\beta$ phase and β phase can be expressed by Eq.(18) and Eq.(19), respectively:

$$E(\varepsilon,\dot{\varepsilon})=13.981\,28-10.061\,1\varepsilon+2.922\,33\varepsilon^2-0.628\,22\ln\dot{\varepsilon}-0.033\,17(\ln\dot{\varepsilon})^2+0.300\,48\varepsilon\ln\dot{\varepsilon} \tag{18}$$

$$E(\varepsilon,\dot{\varepsilon})=9.086\,63-7.200\,36\varepsilon+10.475\,64\varepsilon^2-0.349\,15\ln\dot{\varepsilon}-0.022\,4(\ln\dot{\varepsilon})^2-0.0655\varepsilon\ln\dot{\varepsilon} \tag{19}$$

2.3.4 Determination of $A(\dot{\varepsilon}, \varepsilon, T)$

According to Eq. (13), $[\ln A(\dot{\varepsilon},\varepsilon,T)-\frac{Q(\dot{\varepsilon},\varepsilon,T)}{RT}]$ can be obtained from the intercept of $\ln\{\sinh[\alpha(\varepsilon, T)\sigma]\}$ -ln$\dot{\varepsilon}$ curves under different conditions, and it is recorded as $S(\varepsilon, T)$. The variation of $S(\varepsilon, T)$ at different strains and temperatures is calculated, as shown in Fig. 8. It can be seen that $S(\varepsilon, T)$ is very sensitive to strain and temperature, so it is considered as a function of temperature and strain. The correlation coefficients of S value in $\alpha+\beta$ phase and β phase are R_1= 0.9765 and R_2=0.9647, respectively. Therefore, $S(\varepsilon, T)$ in $\alpha+\beta$ phase and β phase can be expressed by Eq. (20) and Eq. (21), respectively:

$$S(\varepsilon,T)=-248.675\,05+12.372\,82\varepsilon+0.470\,94T-4.006\,34\varepsilon^2-2.280\,31\times10^{-4}T^2-0.008\,41\varepsilon T \tag{20}$$

$$S(\varepsilon,T)=51.570\,16+3.181\,29\varepsilon-0.097\,01T-0.796\,08\varepsilon^2-4.131\,34\times10^{-5}T^2-0.003\,18\varepsilon T \tag{21}$$

By substituting $Q(\dot{\varepsilon},\varepsilon,T)$ from Eq.(17) into $[\ln A(\dot{\varepsilon},\varepsilon,T)]-\frac{Q(\dot{\varepsilon},\varepsilon,T)}{RT}$, Eq.(22) can be obtained, as follows:

$$\ln A(\dot{\varepsilon},\varepsilon,T)=S(\varepsilon,T)+\frac{1000n(\varepsilon,T)E(\varepsilon,\dot{\varepsilon})}{T} \tag{22}$$

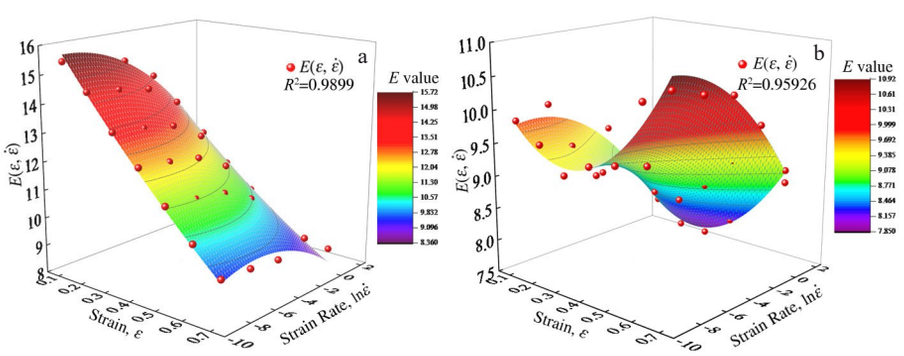

Fig.7 3D images of $E(\varepsilon,\dot{\varepsilon})$ values and curved surface regression fitting results in $\alpha+\beta$ phase (a) and β phase (b)

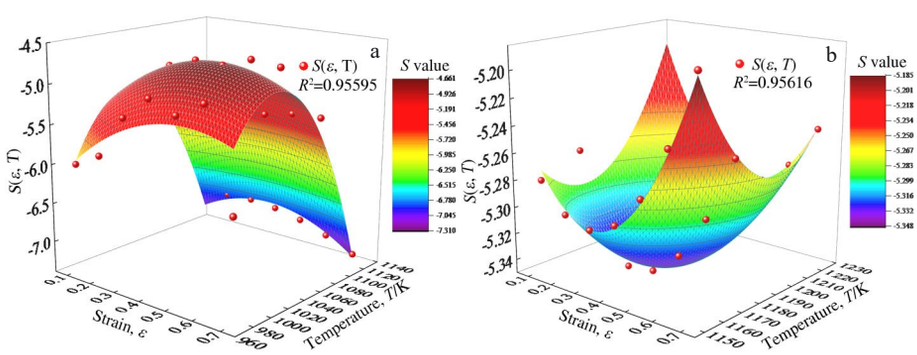

Fig.8 3D images of $S(\varepsilon, T)$ values and curved surface regression fitting results in $\alpha+\beta$ phase (a) and β phase (b)

According to the calculation results, the flow behavior of the Ti-55511 alloy during hot deformation can be expressed by the correction model with activation energy evolution, as shown in Eq.(7–22).

2.4 BP-ANN model

BP-ANN is an artificial intelligence algorithm by the backward propagation learning algorithm[38]. Compared with the physical-based constitutive model, the BP-ANN model does not need to establish a complex mathematical model system, which provides a new method to predict the flow stress behavior of alloys during the hot plastic deformation[39]. The Matlab Neural-Net-Fitting application was used to establish BP-ANN model for prediction. As shown in Fig. 9, the structure of BP-ANN model contains an input layer, an output layer, and some hidden layers. The function of the input layer is to accept the output layer signal. In this model, the input layer has three nodes: temperature, strain rate, and strain. The output layer has only a node: the flow stress σ. The hidden layer connects the input layer to the output layer, and the output layer generates the output signal. The number of nodes in the hidden layers can be calculated by Eq. (23), as follows:

$$N = \sqrt{n + m} + k \tag{23}$$

where n is the number of input layer nodes, m is the measured stress, and k is the integer from 2 to 10.

Fig. 10 shows the relationship between root mean square error (R_{MSE}) and the number of hidden layer nodes. R_{MSE} can be calculated by Eq.(24), as follows:

$$R_{MSE} = \sqrt{\frac{1}{N}\sum_{i=1}^{N}(E_i - P_i)} \tag{24}$$

where E_i is the experiment value of specimen i; P_i is the predicted value of specimen i; N is the total number of specimens.

It can be seen that R_{MSE} of the training set is decreased significantly with increasing the number of neurons. When the number of neurons in the hidden layer is 12, the R_{MSE} value reaches the minimum. Therefore, it can be determined that the optimal neuron number of the neural network model is 12, and k=10.

The strain-stress data in different phase regions were trained. The "trainbr" function and "learngd" function were used for the training and learning, respectively. Meanwhile, the "Tansig" function was used for the hidden layer transfer and the "Purelin" function was used for output layer. In addition, 75% data were randomly selected for training specimens, 15% data were selected for validation, and others were set as test specimens. The input data have a significant difference in orders of magnitude and units, therefore reducing the convergence speed and prediction accuracy[40]. Thus, the input data must be treated through dimensionless normalization to eliminate the influence. The normalization and non-normalization equations are expressed by Eq.(25) and Eq.(26), respectively:

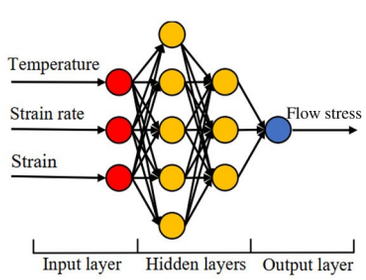

Fig.9 Schematic diagram of BP-ANN model

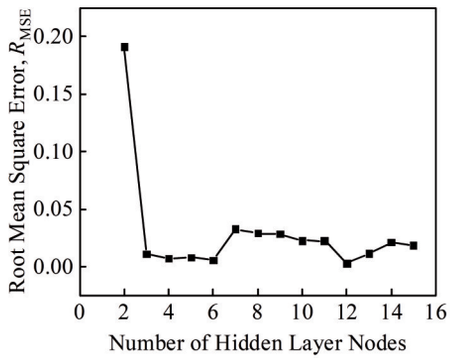

Fig.10 Relationship between root mean square error R_{MSE} and the number of hidden layer nodes

$$y = 0.1 + 0.8\frac{x - x_{min}}{x_{max} - x_{min}} \tag{25}$$

$$y = x_{min} + 1.25(x_{max} - x_{min})(y - 0.1) \tag{26}$$

where x is the initial input data; x_{min} and x_{max} are the minimum and maximum value of initial data, respectively; y is normalized data.

3 Results and Discussion

A good constitutive model not only can well fit the modeling data but also can accurately predict the flow stress under other deformation conditions. Therefore, the data used for model establishment and the load of thermal compression were calculated and compared. The stresses predicted by the corrected Arrhenius model and BP-ANN model were compared with the experiment stress under different deformation conditions, as shown in Fig. 11. It can be observed that the stresses predicted by the modified Arrhenius model and BP-ANN model are all in good agreement with the experiment stresses under different conditions.

To further compare the accuracy of the two constitutive models, two statistical indexes, correlation coefficient (R) and average absolute relative error (AARE), were used as the evaluation criteria in this research, which can be expressed by Eq.(27) and Eq.(28), respectively:

$$R^2 = \frac{\sum_{i=1}^{N}(E_i - \bar{E})}{\sqrt{\sum_{i=1}^{N}(E_i - \bar{E})^2 \sum_{i=1}^{N}\sum_{i=1}^{N}(P_i - \bar{P})^2}} \tag{27}$$

$$\mathrm{AARE} = \frac{1}{N}\sum_{i=1}^{N}\left|\frac{E_i - P_i}{e}\right| \times 100\% \tag{28}$$

where $\bar{E}$ is the average value of E_i and $\bar{P}$ is the average value

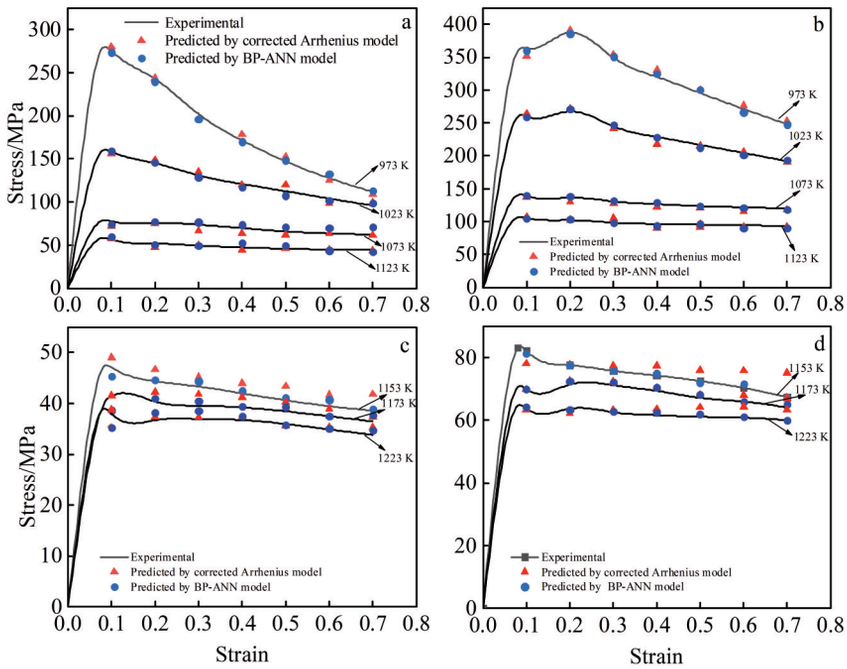

Fig.11 Comparisons of experimental and predicted stresses at strain rates of 0.01 s^{-1} (a, c) and 0.1 s^{-1} (b, d) in $\alpha+\beta$ phase (a, b) and β phase (c, d)

of P_i.

Fig.12 shows the comparison results of corrected Arrhenius model and BP-ANN model. It can be found that most data points can well coincide with the fitting line. In the $\alpha+\beta$ phase region, the R^2 and AARE values of the corrected Arrhenius model are 0.998 95 and 2.7542%, respectively. In the β phase region, the R^2 and AARE values are 0.9807 and 3.9842%, respectively. The R^2 and AARE values of the BP-ANN model in $\alpha+\beta$ phase region are 0.998 95 and 1.9812%, respectively, and they are 0.9912 and 2.216 22% in β phase region, respectively. Therefore, in all phase region, the BP-ANN model shows better correlation and prediction accuracy than the corrected Arrhenius model does overall.

The accuracy of the corrected strain-stress curves can be further evaluated by finite element simulation. In this research, the corrected Arrhenius model and BP-ANN model were used to predict the stress-strain data of Ti-55511 alloy during compression processes at 1023 and 1153 K through

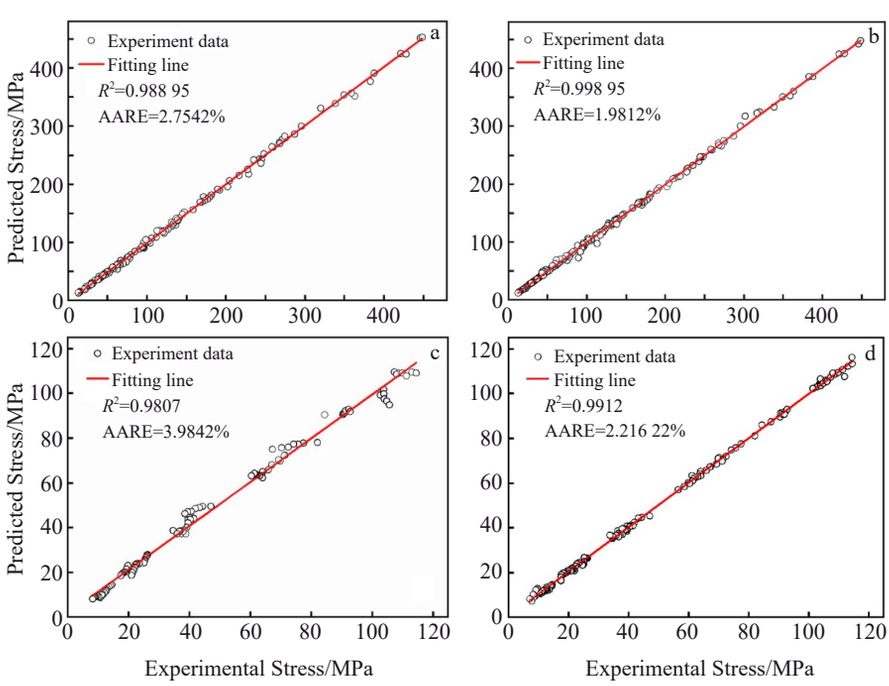

Fig.12 Comparison of experimental and predicted stresses by corrected Arrhenius model (a, c) and BP-ANN model (b, d) in $\alpha+\beta$ phase (a, b) and β phase (c, d)

Fig.13 Schematic diagram of hot compression simulation model

DEFORM-2D finite element software. Fig. 13 shows the schematic diagram of hot compression simulation model. Only a representative plane was used for cylindrical compression. The workpiece was set as a plastic body and the two anvils were set as rigid bodies. The initial size of workpiece was Φ10 mm×12 mm. The shear friction coefficient between anvil and workpiece was 0.3, and the heat-exchange with environment was ignored.

Fig. 14 presents the relationships between load and die displacement in $\alpha+\beta$ phase and β phase, and the effective strain field and the temperature field of the workpiece can also be observed. The strain of the hot-deformed workpiece ranges from 0.0864 to 2.1300. Due to the friction, the strain field can be roughly divided into three regions: large deformation region, small deformation region, and difficult deformation region. When the die displacement is 4 mm, the strain in large deformation region rises to 0.7 and the temperature rises to 814 and 891 °C in $\alpha+\beta$ phase and β phase, respectively. The temperature increments in $\alpha+\beta$ phase and β phase are close to the values calculated by Eq.(4) and Eq.(5), respectively, which indicates the correctness of temperature correction. The variation trend of load is basically consistent with the experimental results, suggesting that the two models are valid and feasible to simulate the hot compression process of Ti-55511 alloy. Moreover, in $\alpha+\beta$ phase and β phase, AARE values of corrected Arrhenius model are 5.7078% and 4.6157%, whereas those of BP-ANN model are 3.9274% and 5.169%, respectively. Therefore, in $\alpha+\beta$ phase region, the prediction accuracy of BP-ANN model is higher than that of corrected Arrhenius model. The BP-ANN model can be used to predict the stress-strain data and the simulation accuracy can be improved by reducing the interpolation interval.

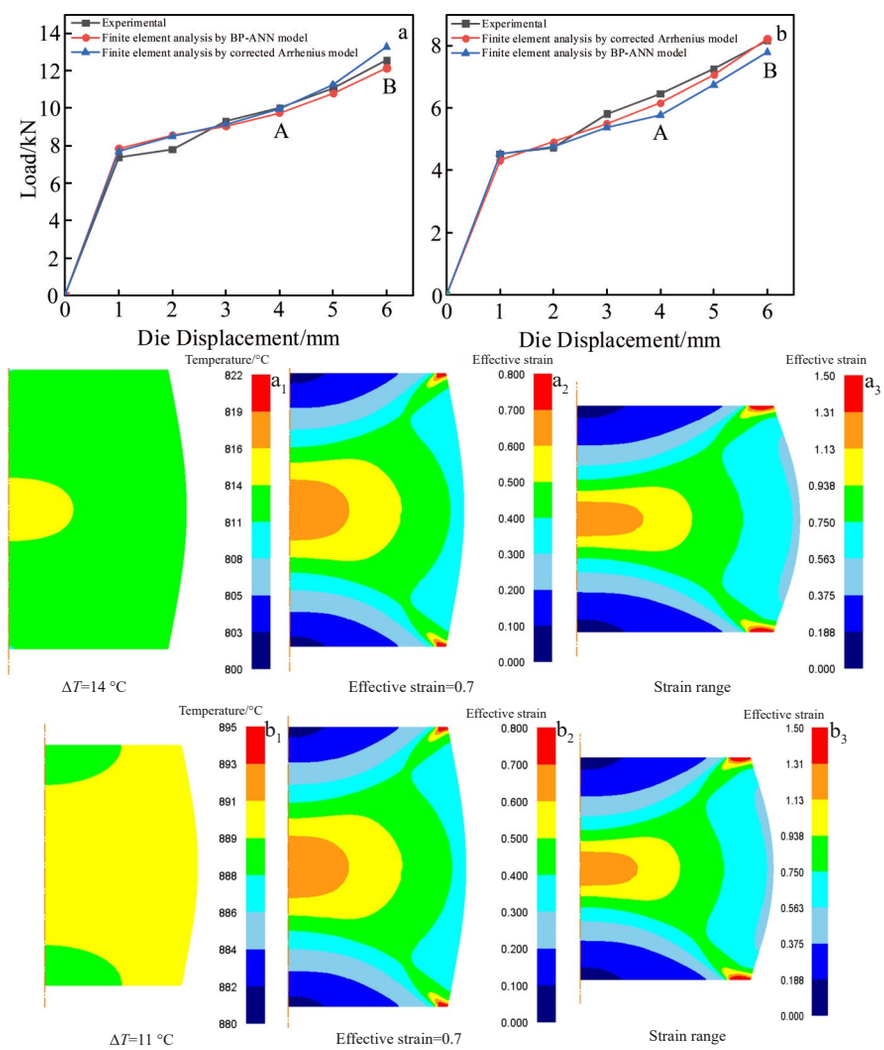

Fig.14 Relationships between load and die displacement in $\alpha+\beta$ phase (a) and β phase (b); temperature distributions (a_1, b_1) and effective strain distributions (a_2, b_2) at effective strain=0.7 in $\alpha+\beta$ phase (a_1–a_2) and β phase (b_1–b_2); effective strain distribution at final deformation stage in $\alpha+\beta$ phase (a_3) and β phase (b_3)

However, in β region, the accuracy of BP-ANN model is lower because of the over-fitting in model training. In β phase region, the corrected Arrhenius model shows higher prediction accuracy.

4 Conclusions

1) The flow stress of Ti-55511 alloy is very sensitive to the deformation temperature and strain rate, and it is positively related to strain rate and negatively related to the deformation temperature. The stress-strain curve has different trends in $\alpha+\beta$ phase and β phase regions because of the phase transformation and recrystallization. Dynamic softening occurs in $\alpha+\beta$ phase region. With increasing the strain, the flow stress is firstly increased to the peak value and then decreased. The softening mechanism is primarily caused by recrystallization. The stress-strain curve enters into the steady state in β phase region.

2) The temperature rise by adiabatic heating is more obvious at high strain and low deformation temperature. The friction during hot deformation causes the higher measured data than the actual data. The difference becomes more obvious with increasing the strain. Finite element simulation of temperature field and load proves the correctness of stress correction.

3) Both the corrected Arrhenius model and the back-propagation artificial neural network (BP-ANN) model can describe the flow behavior of Ti-55511 alloy. Overall, BP-ANN model has higher accuracy than the corrected Arrhenius model to predict the flow stress. In $\alpha+\beta$ phase region, BP-ANN model has higher accuracy. But in β phase region, the corrected Arrhenius model has better prediction results. The simulation accuracy of BP-ANN model can be improved by reducing the interpolation interval.

References

1 Fan R L, Yong W U, Chen M H *et al*. *Transactions of Nonferrous Metals Society of China*[J], 2020, 30(4): 928

2 Fan X G, Zeng X, Yang H *et al*. *Transactions of Nonferrous Metals Society of China*[J], 2017, 27(11): 2390

3 Ning Y Q, Xie B C, Liang H Q *et al*. *Materials and Design*[J], 2015, 71: 68

4 Li Shaoqiang, Gong Zhanpeng, Li Hui *et al*. *Rare Metal Materials and Engineering*[J], 2020, 49(9): 3045 (in Chinese)

5 Ren Dechun, Su Huhu, Zhang Huibo *et al*. *Acta Metallurgica Sinica*[J], 2019, 55(4): 480 (in Chinese)

6 Dai S J, Yu W, Ng C F *et al*. *Materials Science and Engineering A*[J], 2013, 575: 35

7 Zhang Zhiqiang, Dong Liming, Guan Shaoxuan *et al*. *Acta Metallurgica Sinica*[J], 2017, 53(4): 415 (in Chinese)

8 Luo S Y, Yao J N, Li J *et al*. *Journal of Materials Research and Technology*[J], 2020, 9(6): 12 043

9 Tetyukhin V V, Leder M O, Kropotov V A *et al*. *Proceedings of the 13th World Conference on Titanium*[C]. San Diego: TMS, 2016

10 Luo S Y, Yao J N, Zou G M *et al*. *Journal of Materials Research and Technology*[J], 2020, 9(4): 8235

11 Wu C, Zhan M. *Journal of Alloys and Compounds*[J], 2019, 805: 1144

12 Dai X, Wen C, Wu L *et al*. *Chinese Journal of Aeronautics*[J], 2021, 34(11): 228

13 Fan J K, Zhang Z X, Gao P Y *et al*. *Journal of Materials Science & Technology*[J], 2020, 38: 135

14 Lu L L, Zhang Y M, Zhang Z L *et al*. *Materials Research Express*[J], 2021, 8(9): 96 520

15 Liu Z G, Li P J, Xiong L T *et al*. *Materials Science and Engineering A*[J], 2016, 680: 259

16 Pilehva F, Zarei-Hanzaki A, Moemeni S *et al*. *Journal of Materials Engineering & Performance*[J], 2016, 25(1): 46

17 Zhang Xiaolin, Jiang Chaoping, Zhao Ddong *et al*. *Rare Metal Materials and Engineering*[J], 2022, 51(1): 174 (in Chinese)

18 Huang L G, Chen Y Y, Kong F T *et al*. *Materials Science and Engineering A*[J], 2013, 577: 1

19 Li Huiming, Zhang Jingli, Mao Xiaonan *et al*. *Rare Metal Materials and Engineering*[J], 2021, 50(6): 1980 (in Chinese)

20 Tabei A, Abed F H, Voyiadjis G Z *et al*. *European Journal of Mechanics-A/Solids*[J], 2017, 63: 128

21 Matsumoto, H, Velay V. *Journal of Alloys and Compounds*[J], 2017, 708: 404

22 Chanfreau N, Poquillon D, Stark A *et al*. *Journal of Materials Science*[J], 2022, 57(9): 5620

23 Liang R Q, Khan A S. *International Journal of Plasticity*[J], 1999, 15(9): 963

24 Chen Liquan, Yang Quan, Li Zhishang *et al*. *Rare Metal Materials and Engineering*[J], 2021, 50(10): 3600 (in Chinese)

25 Hajari A, Morakabati M, Abbasi S M *et al*. *Materials Science and Engineering A*[J], 2016, 681: 103

26 Mosleh A, Mikhaylovskaya A, Kotov A *et al*. *Metals*[J], 2017, 7(12): 568

27 Yang X M, Guo H Z, Liang H Q *et al*. *Journal of Materials Engineering and Performance*[J], 2016, 25(4): 1347

28 Wen T, Liu L T, Huang Q *et al*. *Journal of Central South University*[J], 2018, 25(6): 1251

29 Quan G Z, Zhang P, Ma Y Y *et al*. *Transactions of Nonferrous Metals Society of China*[J], 2020, 30(9): 2435

30 Quan G Z, Wen H R, Pan J *et al*. *International Journal of Precision Engineering and Manufacturing*[J], 2016, 17(2): 171

31 Li Q, Jin C Y. *Rare Metal Materials and Engineering*[J], 2021, 50(11): 3924

32 Lei Yu, Xu Nianao, Zhang Chenjie *et al*. *Rare Metal Materials and Engineering*[J], 2020, 49(12): 4192 (in Chinese)

33 Long S, Xia Y F, Wang P *et al*. *Journal of Alloys and Compounds*[J], 2019, 796: 65

34 Ebrahimi R, Najafizadeh A. *Journal of Materials Processing Technology*[J], 2004, 152(2): 136

35 Goetz R L, Semiatin S L. *Journal of Materials Engineering and Performance*[J], 2001, 10(6): 710
36 Zhang J S, Xia Y F, Quan G Z *et al*. *Journal of Alloys and Compounds*[J], 2018, 743: 464
37 Mataya M C, Sackschewsky V E. *Metallurgical and Materials Transactions A*[J], 1994, 25(32): 2737
38 Luo R, Cao Y, Cui S G *et al*. *Transactions of the Indian Institute of Metals*[J], 2021, 74(7): 1809
39 Huang C Q, Jia X D, Zhang Z W. *Materials*[J], 2018, 11(5): 13
40 Lin Y C, Nong F Q, Chen X M *et al*. *Vacuum*[J], 2017, 137: 104

基于材料参数演化修正Arrhenius模型与BP-ANN模型的近β Ti-55511合金等温压缩过程流动应力预测

滕海灏，夏玉峰，孙　涛，郑德宇，陈　磊
(重庆大学 材料科学与工程学院，重庆 400044)

摘　要：为了研究Ti-55511合金在近β区域的热流动行为，在温度973–1223 K、应变速率0.001–1 s^{-1}条件下，利用Gleeble−3500热模拟试验机进行了等温压缩试验。对实验获得的流动应力曲线进行了修正，降低了摩擦与绝热温升等因素对流动应力的影响。采用考虑材料参数演化的修正Arrhenius模型和反向传播人工神经网络（BP-ANN）模型对钛合金热变形过程中的流动应力进行预测，并通过统计分析对预测模型精度进行了评估。将2种预测模型扩展的应力、应变数据植入有限元，模拟了热压缩实验过程。结果表明，Ti-55511合金的流变应力与应变速率呈正相关，与温度呈负相关，合金软化机制主要为再结晶。修正后的Arrhenius模型和BP-ANN模型都能描述流体的流动行为，BP-ANN模型在α+β区域的拟合精度高于修正后的Arrhenius模型，而在β区域的拟合精度低于修正后的Arrhenius模型。

关键词：本构模型；Ti-55511合金；流动应力；修正Arrhenius模型；BP-ANN模型

作者简介：滕海灏，男，1996年生，博士生，重庆大学材料科学与工程学院，重庆 400044，E-mail：tenghaihao1996@163.com